Ionics
https://doi.org/10.1007/s11581-025-06416-9

RESEARCH

Experimental and DFT calculations for C/ZnO@S cathode and prelithiation Si anode for advanced sulfur-based batteries

Maryam Sadat Kiai[1,2] · Navid Aslfattahi[3] · Mubashir Mansoor[4] · Deniz Karatas[5] · Nilgun Baydogan[6] · Lingenthiran Samylingam[7] · Kumaran Kadirgama[8,9,10] · Chee Kuang Kok[7]

Received: 31 March 2025 / Revised: 18 May 2025 / Accepted: 20 May 2025

Abstract

The advancement of modified electrodes for the next generation of sulfur-based batteries has become a prominent focus of research. This study introduces a detailed DFT calculations for the cell with carbon-doped ZnO/S as a potential cathode material through urea-assisted thermal decomposition of zinc acetate. Ultralong cycling stability is achieved after 500 cycles at 2 C for C-doped ZnO, resulting in an impressive reversibility of 981 mAh g^{-1}, with a capacity retention of 86.2% and minimal capacity degradation of just 0.023% per cycle. The carbon-doped ZnO/LiS_2 model has a higher electrical conductivity compared to the Li_2S/ZnO model. The DFT result proved the strong interaction of silicon with both carbon and oxygen; subsequently, the interaction in ZnO models containing SiS_2 was much higher, especially in the model containing carbon, which is in good agreement with our experiments.

Keywords Batteries · ZnO · Carbon doping · Cycle stability · DFT · Catalytic properties

Introduction

In recent years, lithium-sulfur (Li–S) batteries have emerged as a promising alternative for next-generation energy storage solutions, owing to their significant advantages, such as a high theoretical capacity of 1675 mAh g^{-1}, along with cost-effectiveness and environmental sustainability. However, the implementation of Li–S batteries encounters several technical challenges, including the poor electrical conductivity of sulfur and the discharge product lithium sulfide (Li_2S), and pronounced shuttling behavior caused by the dissolution of lithium polysulfides (LiPSs) [1–4]. These technical hurdles lead to reduced sulfur utilization, slow reaction kinetics, rapid capacity degradation, and severe corrosion

✉ Navid Aslfattahi
navid.fth87@yahoo.com; navid.aslfattahi@fs.cvut.cz

✉ Kumaran Kadirgama
kumaran@umpsa.edu.my

1 Center for BioNano Interactions, School of Chemistry, University College of Dublin, Belfield, Dublin 4, Ireland

2 Nano-Science and Nano-Engineering Program, Graduate School of Science, Engineering and Technology Istanbul Technical University Istanbul, Istanbul 34469, Turkey

3 Department of Fluid Dynamics and Thermodynamics, Faculty of Mechanical Engineering, Czech Technical University in Prague, Prague 166 07, Czech Republic

4 Metallurgical and Materials 813 Engineering Department and Department of Applied Physics, 814 Istanbul Technical University, 34469 Istanbul, Turkey

5 Bioengineering Department, Manisa Celal Bayar University, Yunusemre, Manisa 45140, Turkey

6 Energy Institute, Ayazaga Campus Istanbul Technical University Maslak, Istanbul, Turkey

7 Center for Advanced Mechanical and Green Technology, Center of Excellence for Robotics & Sensing Technologies, Faculty of Engineering and Technology, Multimedia University, Jalan Ayer Keroh Lama, 75450 Bukit Beruang, Melaka, Malaysia

8 Faculty of Mechanical & Automotive Engineering Technology, University Malaysia Pahang Al-Sultan Abdullah, 26600 Pekan, Pahang, Malaysia

9 Centre for Research in Advanced Fluid and Processes, University Malaysia Pahang Al-Sultan Abdullah, 26600 Pekan, Pahang, Malaysia

10 Centre for Sustainable Materials & Surface Metamorphosis (CSMSM), Chennai Institute of Technology, Chennai, India

of the anode in Li–S batteries. The employment of lithium metal as an anode material presents significant challenges, primarily due to its high reactivity with electrolyte solvents and salts, as well as its propensity to form dendrites. These factors contribute to a reduced operational lifespan and pose considerable safety risks, highlighting the need for the exploration of alternative anode materials for practical use [5–12]. Recently, silicon (Si) alloy-type anodes have garnered significant interest owing to their cost-effectiveness and abundant availability in the earth's crust. The integration of Si with sulfur in a full cell configuration may provide a promising avenue for the advancement of next-generation high-energy storage systems. [13–19] For silicon anodes, it is essential to address volume fluctuations and to create a stable solid electrolyte interphase (SEI).

Additionally, carbon-based nanostructured materials have been extensively investigated for their potential in the cathode to mitigate lithium polysulfides (LiPSs) due to their advantageous properties, including excellent electrical conductivity, large surface area, and porous structures. However, these materials exhibit limited capacity for LiPS absorption, leading to inadequate cycling stability attributed to the persistent shuttle effect [20–23]. Recently, significant advancements have been made with polar materials that serve as effective adsorbents for LiPSs, including TiO_2, ZnO, CoS, MoS_2, and Co_3S_4. Despite these developments, the metal oxide components mentioned often possess low electrical conductivity, which restricts their catalytic efficiency towards LiPSs and ultimately impedes electron and ion transport, resulting in suboptimal rate performance [24–28].

In this study, we present a DFT study for carbon-doped (C) ZnO/S as a promising cathode material to facilitate redox reactions and improve cycling performance for pre-lithiation Si/S batteries. The DFT results proved the role of C-doped ZnO for polysulfide trapping as a cathode for pre-lithiation silicon-sulfur batteries.

In this study, SiS_2 and Li_2S binding energy on carbon-doped ZnO and pristine ZnO surfaces was investigated with DFT using the TURBOMOLE 7.8.1 program. All DFT calculations were performed with the PBE/def2-TZVP basis set. Single-point energy and adsorption energies of the optimized structures were obtained as a result of geometry optimization.

Experimental section

Synthesis of carbon-doped ZnO/S

Carbon-doped ZnO was prepared by thoroughly grinding 15 g of sulfur (S), 4 g of zinc acetate dihydrate (Zn $(Ac)_2 \cdot 2H_2O$), and 1 g of urea in a mortar for a duration of 30 min. Subsequently, the resulting powders were subjected to annealing in an alumina crucible at a temperature of 500 °C, with a heating rate of 20 °C per minute, for a period of 3 h in an air atmosphere. Upon completion of the reaction, the powders were rinsed with distilled water and then dried in an oven at 70 °C for 12 h. The final product with 10% C doped ZnO was designated as C/ZnO@S [29].

New active sites were formed with the carbon doping, and -CS, -SiC bonds were formed.

Synthesis of Si@GNP anode

Si/GNP nanostructure was obtained by dispersing Si NPs into an aqueous solution of GNP, followed by a hydrothermal process. Typically, 7.5 g GNP were dissolved in 100 mL deionized water to form a homogeneous solution. After adding 0.1 g Si NPs into the above solution, the mixture was stirred for 1 h. The mixture was then transferred into a 100-mL Teflon-lined autoclave and kept at 150 °C for 12 h, subsequently followed by vacuum filtration, washing with DI water. Before utilization, the Si@GNP electrode underwent a chemical pre-lithiation process through surface treatment conducted within an argon-filled glovebox. [29] The electrode disk was then placed in contact with a lithium foil that had been moistened with a 1 M solution of $LiPF_6$ in a mixture of ethylene carbonate and dimethyl carbonate (EC/DMC; 1:1 w/w) and subjected to a pressure of 1 bar for a duration of 2 h. Subsequently, the electrode was rinsed with DOL and prepared for use.

Cell configuration

Coin-type 2032 Li–S cells were constructed within an argon-filled glovebox. In this study, a 1 M solution of bis(trifluoromethane)sulfonamide lithium (LiTFSI) combined with 0.5 M lithium nitrate ($LiNO_3$) was evaluated as an effective electrolyte for the entrapment of polysulfides. The solvent system utilized was a 1:1 mixture of 1,3-dioxolane (DOL) and 1,2-dimethoxyethane (DME). The electrolyte volume in various coin cells was standardized at 20 μL per milligram of sulfur. Our cells contained C/ZnO@S cathode and Si@GNP anode.

Materials and electrochemical characterization

XRD diffraction analysis is carried out with Rigaku smart lab by using Cu Ka radiation (k = 1.541 Å). Raman analysis was performed by Renishaw Raman Spectroscopy. Elemental compositions were analyzed using X-ray photoelectron spectroscopy (Hemispherical analyzer, K-Alpha XPS). Scanning electron microscopic (Gemini FESEM) and transmission electron microscopic (2100 F TEM) were investigated to understand the morphology of the samples. SEM with energy-dispersive X-ray spectroscopy (EDS) was carried out to scan the distribution of elements. The specific surface area was assessed through nitrogen adsorption and desorption measurements using the Brunauer–Emmett–Teller (BET) multipoint method.

Computational section (DFT)

All DFT calculations were performed with the PBE/def2-TZVP basis set. The binding energy per Li/Si atom (E_{ad}) is calculated using Eq. 1.

$$E_{ad} = \frac{E_{\text{bonded}} - E_{\text{pristine}} - 2\mu_{Li/Si}}{2} \tag{1}$$

E_{bonded} is the total energy of the Li/Si bonded structure, and E_{pristine} is the total energy of the pristine structure without the two Li/Si atoms. $\mu_{Li/Si}$ is the Li/Si chemical potential. [30–32]

The binding energy of the SiS_2 molecule to the ZnO surface was quite strong, and its energy was calculated as − 5.88 eV/Si. The most important first bond formation was included -SiO interaction. The bond lengths here are 1.69 and 1.70 Å (Si-S) The other intermolecular bond formation was between Zn–S, whose distances were calculated as 2.2 and 2.11 Å. With the increase in the surface area with the carbon doping, the adsorption amounts also increased, and its energy was calculated as − 9.01 eV/Si. Similar to the pristine model, one Zn–S bond formation was observed in this model, and the distance was calculated as 2.25 Å. In addition, new active sites were formed with the carbon doping, and -CS, -SiC bonds were formed. Their distances were calculated as 1.98 and 1.88 Å, respectively, which are comparable with other DFT calculated values [33, 34] and is shorter than the bulk wurtzite ZnO bond length of 2.01 Å. This decrease in the bond length in comparison to the bulk wurtzite structure is due to the changes in hybridization from sp3 to sp2 in the monolayer structure. These calculated structural parameters agree with previous experimental and theoretical values [35–37].

Since carbon doping causes surface changes in the molecular structure, it may have also changed the optical, electrical, and catalytic properties of ZnO. In order to understand this, the HOMO–LUMO gaps of the optimized models in Fig. 1 were calculated as + 1.52 and + 1.67 eV with TURBOMOLE, respectively. A HOMO–LUMO gap value of + 1.52 eV indicates that pure ZnO in interaction with SiS_2 exhibits moderate stability and can absorb light within a specific energy range. As can be understood from these relatively small values, it can be said that the molecules are reactive and electron transfer is easy and good conductors.

On the other hand, all DFT studies performed for the SiS_2/ZnO model were also performed for the Li_2S/ZnO model. The final geometries resulting from the geometry optimization are displayed in Fig. 2.

The first important change that is noticeable in Fig. 2 is the strong interactions of lithium atoms with oxygen in both models. While their measurements were calculated as 1 × 1.82 and 2 × 1.87 Å in the pristine ZnO model, these values were calculated as 2 × 1.79 and 1.82 Å in the carbon-filled model. Apart from this, another important interaction is the strong Zn–S bonds seen in the SiS_2/ZnO models, which also appeared in this model, and their measurements were found as 2.31 Å in the pristine model and 2.42 and 2.56 Å in the other model. All these changes significantly affected the binding energy values, and the interaction energy value calculated as − 2.52 eV/Li in the pristine model increased in the presence of carbon and was recorded as − 4.68 eV/Li. As a result of the strong interaction of silicon with both carbon

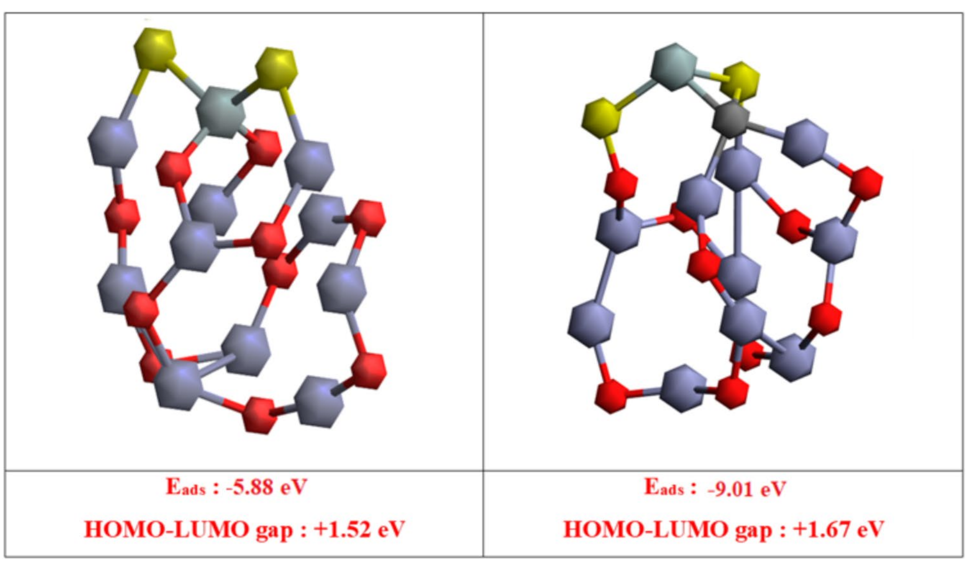

Fig. 1 Optimized pristine (left) and C-doped (right) ZnO structures. Purple, red, yellow, gray, and black colors represent zinc (Zn), oxygen (O), sulfur (S), silicon (Si), and carbon (C), respectively

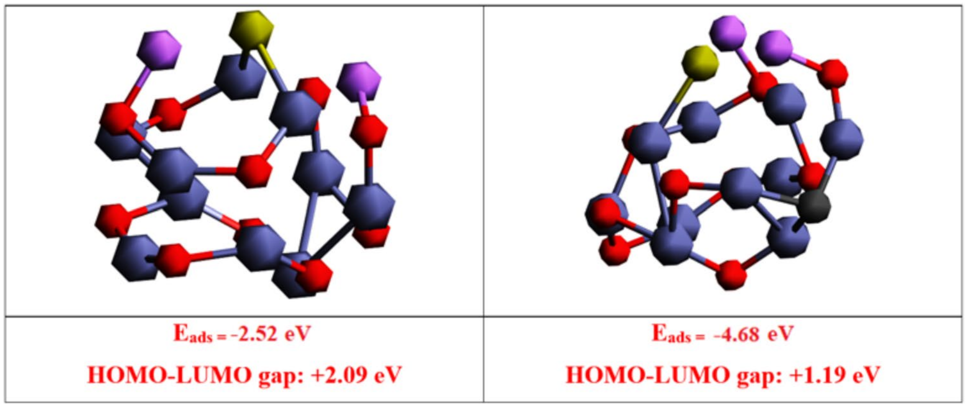

Fig. 2 Optimized pristine (left) and C-doped (right) ZnO structures. Purple, pink, red, yellow, and gray colors represent zinc (Zn), lithium (Li), oxygen (O), carbon (C), and silicon (Si), respectively

and oxygen, the interaction in ZnO models containing SiS_2 was much higher, especially in the model containing carbon. On the other hand, the HOMO–LUMO gap value (+ 1.19 eV) of the carbon-doped ZnO/LiS_2 model was lower than the Li_2S/ZnO model (+ 2.09 eV). Carbon doping changed the electronic structure of the ZnO/LiS_2 model, affecting the HOMO and LUMO levels and causing the HOMO–LUMO gap to decrease. This could provide better performance for the carbon-doped ZnO/LiS_2 model in applications such as energy storage, photocatalysis, or electronic devices. As expected, the carbon-doped ZnO/LiS_2 model has a higher electrical conductivity compared to the Li_2S/ZnO model. The DFT result proved the strong interaction of silicon with both carbon and oxygen; subsequently, the interaction in ZnO models containing SiS_2 was much higher, especially in the model containing carbon, which is in good agreement with our experiments and proved the reason for the application of Si as an anode in combination with a carbon-doped (C) ZnO/S cathode.

Density of states (DOS) was initially investigated to extract relevant information through molecular dynamics simulations. Consequently, no magnetic properties are detectable in C-doped ZnO. The computed band gap for C doped ZnO is 1.24 eV, which is less than the experimentally determined value of 3.37 eV [38–40] (Fig. 3a).

The inherent lithium mobility on the carbon doped ZnO/S is crucial for its practical use as a cathode material in prelithiation Si-S batteries.Therefore, we investigated the potential diffusion pathways and energy barriers for lithium on as illustrated in Fig. 3b.

The two pathways are H–T_{Zn}–H and H–T_C–H, with associated energy barriers of 0.68 eV and 0.12 eV, respectively.

The lithium can diffuse more rapidly along the groove compared to the space between two adjacent grooves, and the strength of single-atom adsorption for utilizing a material is higher than the adsorption of multiple atoms on the surface, which contributes to the storage capacity. [41, 42]

Experimental section (materials' characterization and electrochemical analysis)

The EIS spectra of the C doped ZnO cell exhibit the lower charge transfer resistance in comparison to the pristine ZnO, suggesting an enhanced kinetic redox reaction for the conversion of polysulfides facilitated by the C-doped ZnO (Fig. 4a).

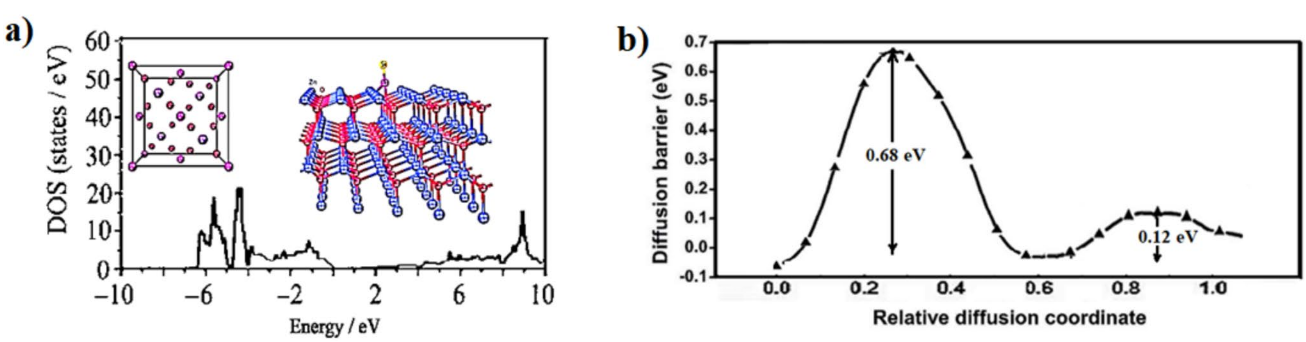

Fig. 3 **a** Atomistic configuration (3D) and DOS for C-doped ZnO derived from DFT. **b** The pathway and energy barriers for Li atoms diffused between two adjacent grooves or inside the grooves

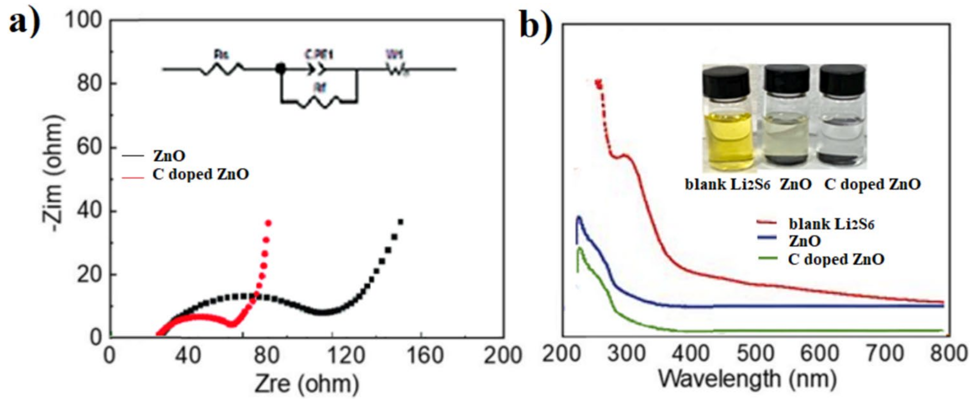

Fig. 4 **a** EIS spectrum of the cells with pristine and C-doped ZnO. **b** Digital photographs of LiPSs adsorption and UV – vis spectrum after immersion in Li_2S_6 solution for 6 h

To visually assess the trapping effect of the synthesized samples on polysulfides, adsorption experiments were conducted using Li_2S_6 solutions at a concentration of 5 mmol L^{-1}. After immersing the as-prepared materials in glass bottles for 6 h of immersion, the pristine ZnO retained a slight yellow color and C-doped ZnO samples became colorless (Fig. 4b), indicating a significantly stronger chemical affinity of C-doped ZnO for polysulfides compared to pristine ZnO. [43] To further investigate the binding degree of lithium polysulfides (LiPSs), ex situ ultraviolet (UV) spectroscopy was employed (Fig. 4b). The C-doped ZnO sample exhibited a much weaker absorption peak for LiPSs and SiPSs compared to the pristine ZnO sample, demonstrating that the C-doped ZnO sample possesses superior adsorption capacity for Li and Si PSs.

Figure 5a presents the cyclic voltammetry (CV) curves recorded within a voltage range of 1.6 – 2.8 V for the cathode, which is the normal voltage range of the cathode for commercial Li–S cells at a sweep rate of 0.1 mV $s.^{-1}$. [44–46] Notably, two significant negative peaks were observed at 2.32 V (peak I) and 2.12 V (peak II), corresponding to the reduction of S8 to higher-order soluble Li_2S_x (where $4 \le x \le 8$), followed by the reduction to lower-order insoluble Li_2S/Li_2S_2. Furthermore, one sharp positive peak at 2.46 V (peak III) is associated with the oxidation of short-chain Li_2S/Li_2S_2 to long-chain Li_2S_x and S8. [47, 48]

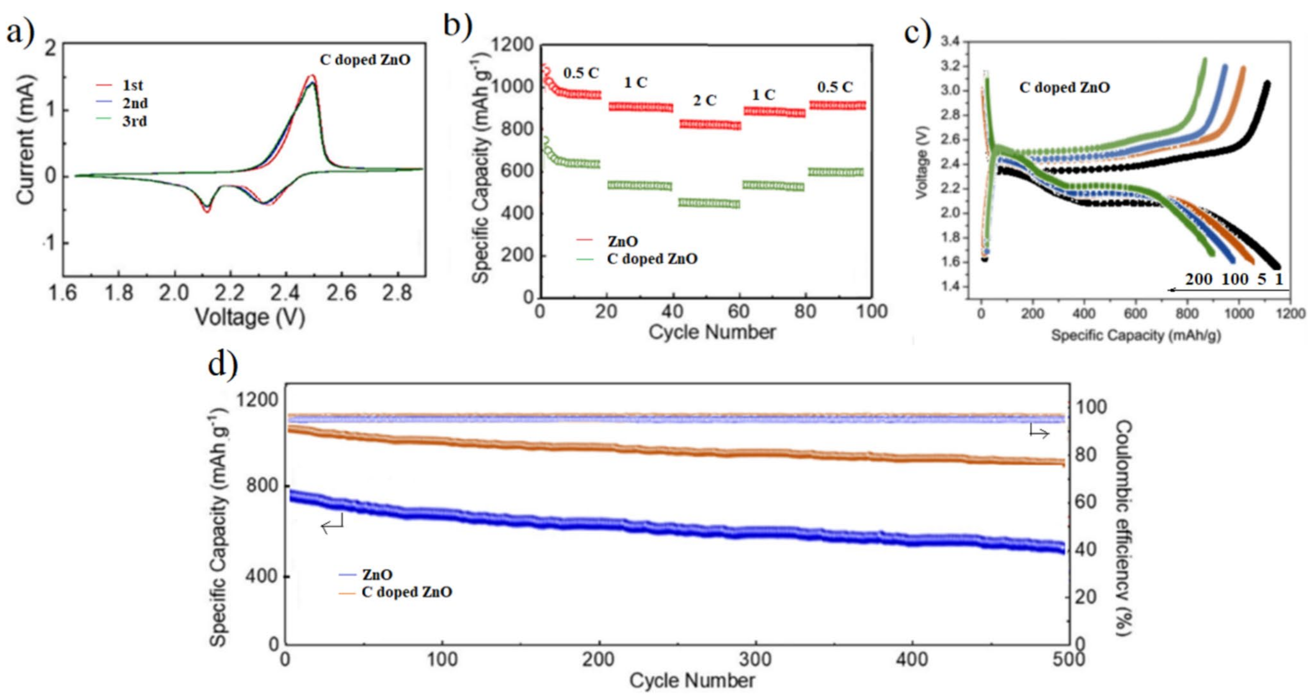

Fig. 5 **a** CV curves for C-doped ZnO at different cycles. **b** Rate capability for the cells with ZnO and C-doped ZnO at different scan rates. **c** Charge discharge voltage curve for the cell with C-doped ZnO at 3 C. **d** Long cycle life for ZnO and C-doped ZnO at 2 C

The performance of batteries utilizing pristine ZnO and C-doped ZnO was further evaluated. The C doped ZnO modified cell demonstrated impressive rate capabilities, achieving capacities of 1046, 938, 871, 918, and 929 mAh g^{-1} at current densities of 0.5, 1, 2, and 1 and 0.5 C, respectively. Additionally, when the current was reduced back to 0.5 C, the reversible capacity was restored to 929 mAh g^{-1}, which represents 89.0% of its original capacity, highlighting its excellent reversibility and robust redox electrochemistry for C-doped ZnO (Fig. 5b).

The charge discharge voltage curve of the cell with C doped ZnO showed high discharge stability with a small fading rate of discharge capacity after 5, 100, and 200 cycles (Fig. 5c).

Additionally, ultralong cycling stability is achieved after 500 cycles at 2 C, for C-doped ZnO resulting in an impressive reversibility of 981 mAh g^{-1}, with a capacity retention of 86.2% and minimal capacity degradation of just 0.023% per cycle. Pristine ZnO demonstrated reversibility of 426 mAh g^{-1}, with a capacity retention of 53.4% and minimal capacity degradation of just 0.092% per cycle (Fig. 5d).

The S K-edge XANES spectra confirm the presence of unoccupied states in the electronic density and the local crystal structure (Fig. 6a). The EXAFS spectrum of Zn K-edge displays one distinct peak, showing no edge shift in both C-doped and pristine ZnO [44]. The Fourier transform of the Zn K-edge EXAFS spectra displays a strong peak at 1.87 and 1.84 Å for C-doped and pristine ZnO respectively, attributed to the Zn–S bond, indicating a strong coupling effect between ZnO and polysulfides (S_x) (Fig. 6b).

The Raman spectrum reveals that the carbon doped ZnO exhibits a G-band at 1798 cm^{-1}, characteristic of sp2 hybridized carbon ($E_{2\,g}$), and a D-band at 1228 cm^{-1}, indicative of sp3 hybridized carbon ($A_{1\,g}$). Furthermore, the observed bands are between 400 and 1000 cm^{-1} associated with the Wurtzite structure of ZnO. This finding confirms the presence of ZnO nanoparticles on the carbon substrates in the carbon doped ZnO (Fig. 6c).

The initial decomposition temperature of C-doped ZnO composite materials was found to be lower than that of pure ZnO, attributed to the robust bonding present in the C-doped ZnO composite material. This bonding facilitates the effective movement of molecular chains (Fig. 6d). The uniform distribution of C-doped ZnO nanoparticles in the sulfur cathode improved thermal stability by acting as a barrier to the movement of small gas molecules.

The chronoamperometry curves obtained from Li_2S_6 symmetric cells exhibit a significantly improved current response compared to cells lacking Li_2S_6. This enhancement is particularly evident during the lithiation and delithiation processes, rather than being attributed to double-layer capacitance Fig. 7a. Notably, both pristine ZnO and C-doped ZnO electrodes demonstrated the pronounced current responses, highlighting their beneficial role in facilitating the redox reactions of lithium and silicon polysulfides.

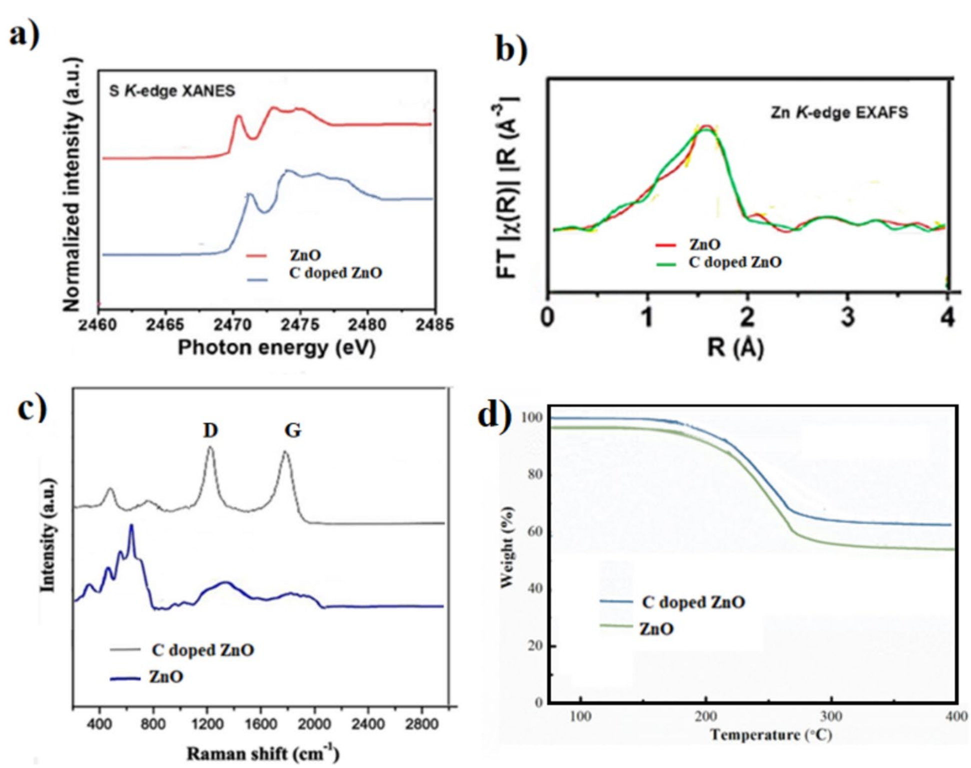

Fig. 6 **a** S K-edge XANES spectrum of the pristine ZnO and C-doped ZnO after cycling, **b** Fourier transforms of Zn K-edge EXAFS spectrum of the pristine ZnO and C-doped ZnO after cycling, **c** Raman spectrum of pristine ZnO and C-doped ZnO after cycling, **d** TGA of C-doped ZnO after cycling

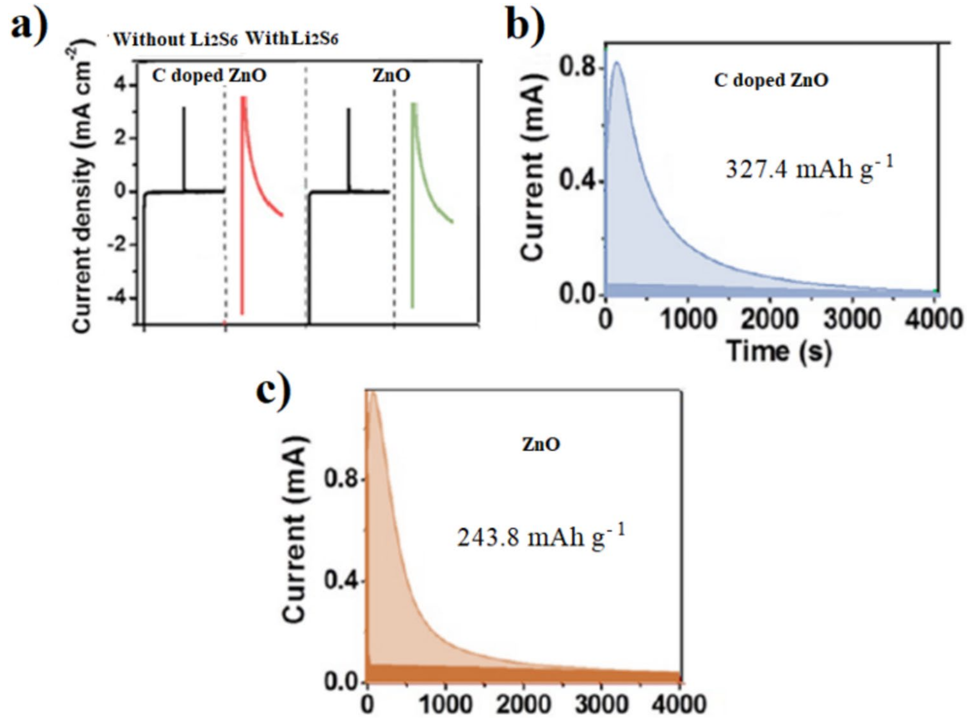

Fig. 7 **a** Chronoamperometric curves of pristine ZnO and C doped ZnO cells. **b** and **c** Potentiostatic discharge profiles of C-doped ZnO and ZnO at 2.0 V

To thoroughly investigate the benefits of heterostructures in the conversion of polysulfides, experiments were conducted to observe the precipitation of Li_2S. Based on Faraday's law, the Li_2S precipitation capacity of the C doped ZnO catalyst (327.4 mAh g^{-1}) is superior to that of the pristine ZnO catalyst (243.8 mAh g^{-1}), suggesting that C doped ZnO demonstrates excellent electrocatalytic activity towards polysulfides and significantly enhances the kinetics of Li_2S redox reactions in sulfur electrochemistry [49] (Fig. 7b and c).

To gain deeper insights into the sulfur redox reaction mechanism of the C-doped ZnO, ex situ XANES measurements of the pre-lithiation Si – S battery were conducted at different voltage states during the initial discharge/charge cycle at a rate of 1 C (Fig. 8a). The S K-edge spectra of the C-doped ZnO show a prominent peak at 2471.5 eV, attributed to the S – S bonds of S8. Additionally, another peak at 2469.0 eV is observed during the discharge, which is linked to the soluble polysulfides (Li_2S_x). The other two peaks at 2472.8 and 2474.7 eV indicate the formation of insoluble Li_2S/Si_2S. During the charging phase, the Li_2S peak disappears, coinciding with the appearance of the PSs peaks between 2.2 and 2.4 V (Fig. 8b). Eventually, a strong S8 peak reappears when the battery is fully charged to 2.6 V. This finding further highlights the role of the C-doped

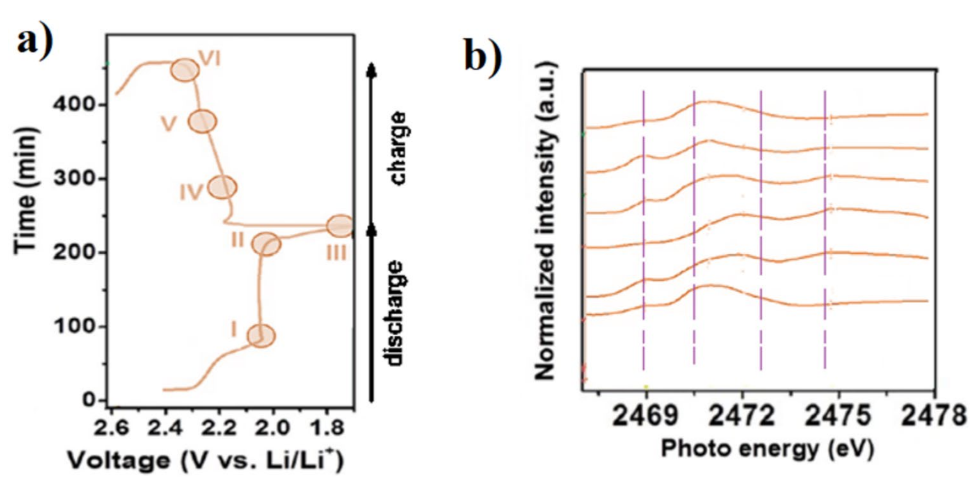

Fig. 8 **a** and **b** Ex situ XANES of sulfur K-edge C-doped ZnO/S cathode at various depths in the first discharge/charge process

ZnO in effectively enhancing the redox kinetics of redox electrochemistry [50–52].

Conclusion

In summary, we present a DFT study for carbon-doped (C) ZnO/S as a promising cathode material to facilitate redox reactions and improve cycling performance for pre-lithiation Si/S batteries. The DFT results proved the role of C-doped ZnO for polysulfide trapping as a cathode for pre-lithiation silicon-sulfur batteries. Since carbon doping causes surface changes in the molecular structure, it may have also changed the optical, electrical, and catalytic properties of ZnO. In order to understand this, the HOMO–LUMO gaps of the optimized models were calculated as + 1.52 and + 1.67 eV with TURBOMOLE, respectively. A HOMO–LUMO gap value of + 1.52 eV indicates that pure ZnO in interaction with SiS_2 exhibits moderate stability and can absorb light within a specific energy range. As can be understood from these relatively small values, it can be said that the molecules are reactive, and electron transfer is easy and good conductors. On the other hand, the HOMO–LUMO gap value (+ 1.19 eV) of the carbon-doped ZnO/LiS_2 model was lower than the Li_2S/ZnO model (+ 2.09 eV). Carbon doping changed the electronic structure of the ZnO/LiS_2 model, affecting the HOMO and LUMO levels and causing the HOMO–LUMO gap to decrease.

Notably, both pristine ZnO and C-doped ZnO electrodes demonstrated the pronounced current responses, highlighting their beneficial role in facilitating the redox reactions of lithium and silicon polysulfides. The DFT results proved the role of C-doped ZnO for polysulfides trapping as a cathode for pre-lithiation silicon-sulfur batteries.

Acknowledgements All authors would like to thank Istanbul Technical University, Istanbul, Manisa Celal Bayar University in Türkiye, University College of Dublin, Ireland, Czech Technical University in Prague, Czech Republic, for resource and technical support.

Author contributions M.S.K. and N.A.; Conceptualisation, formal analysis, methodology, writing—original draft preparation. M.M., D.K., N.B., L.S., K.K. and C.K.K.; writing—review and editing, formal analysis, methodology. M.S.K., N.B.; methodology, writing—original draft preparation, resources. N.A., N.B. and K.K.; resources, supervision, project administration. M.S.K., D.K. and M.M.; software, formal analysis, investigation. All authors have read and agreed to the published version of the manuscript.

Funding Open access publishing supported by the institutions participating in the CzechELib Transformative Agreement.

Data availability Data will be available on a reasonable request from the corresponding author.

Declarations

Conflicts of interest The authors declare no competing interests.

References

1. Kiai MS, Ponnada S, Mansoor M, Aslfattahi N, Naskar S (2023) Synergistic overview and perspectives of two-dimensional heterostructures for cathodes and separators in flexible Li–S batteries. Energy Fuels 37(15):10827–10842
2. Kiai MS, Ponnada S, Eroglu O, Mansoor M, Aslfattahi N, Nguyen V, Gadkari S, Sharma RK (2024) Ti 3 C 2 T x nanosheet@ Cu/Fe-MOF separators for high-performance lithium–sulfur batteries: an experimental and density functional theory study. Dalton Trans 53(1):82–92
3. Zhou G, Zhao S, Wang T, Yang SZ, Johannessen B, Chen H, Liu C, Ye Y, Wu Y, Peng Y, Liu C (2019) Theoretical calculation guided design of single-atom catalysts toward fast kinetic and long-life Li–S batteries. Nano Lett 20(2):1252–1261
4. Eroglu O, Kiai MS, Kizil H (2020) Glass fiber separator coated by boron doped anatase TiO_2 for high-rate Li–S battery. Mater Res Bull 129:110917
5. Chen S, Wu Q, Wen M, Wu Q, Li J, Cui Y, Pinna N, Fan Y, Wu T (2018) Sea-sponge-like structure of nano-Fe_3O_4 on skeleton-C with long cycle life under high rate for Li-ion batteries. ACS Appl Mater Interfaces 10(23):19656–19663
6. Yao Y, Wang H, Yang H, Zeng S, Xu R, Liu F, Shi P, Feng Y, Wang K, Yang W, Wu X (2020) A dual-functional conductive framework embedded with TiN-VN heterostructures for highly efficient polysulfide and lithium regulation toward stable Li–S full batteries. Adv Mater 32(6):1905658
7. Liu YT, Han DD, Wang L, Li GR, Liu S, Gao XP (2019) NiCo2O4 nanofibers as carbon-free sulfur immobilizer to fabricate sulfur-based composite with high volumetric capacity for lithium–sulfur battery. Adv Energy Mater 9(11):1803477
8. Lee SK, Oh SM, Park E, Scrosati B, Hassoun J, Park MS, Kim YJ, Kim H, Belharouak I, Sun YK (2015) Highly cyclable lithium–sulfur batteries with a dual-type sulfur cathode and a lithiated Si/SiOx nanosphere anode. Nano Lett 15(5):2863–2868
9. Mo R, Lei Z, Rooney D, Sun K (2019) Anchored monodispersed silicon and sulfur nanoparticles on graphene for high-performance lithiated silicon-sulfur battery. Energy Storage Mater 23:284–291
10. Wang J, Liao L, Lee HR, Shi F, Huang W, Zhao J, Pei A, Tang J, Zheng X, Chen W, Cui Y (2019) Surface-engineered mesoporous silicon microparticles as high-Coulombic-efficiency anodes for lithium-ion batteries. Nano Energy 61:404–410
11. An W, Gao B, Mei S, Xiang B, Fu J, Wang L, Zhang Q, Chu PK, Huo K (2019) Scalable synthesis of ant-nest-like bulk porous silicon for high-performance lithium-ion battery anodes. Nat Commun 10(1):1447

12. Kwon HJ, Hwang JY, Shin HJ, Jeong MG, Chung KY, Sun YK, Jung HG (2019) Nano/microstructured silicon–carbon hybrid composite particles fabricated with corn starch biowaste as anode materials for li-ion batteries. Nano letters 20(1):625–635
13. Zubair U, Amici J, Crespiera SM, Francia C, Bodoardo S (2019) Rational design of porous carbon matrices to enable efficient lithiated silicon sulfur full cell. Carbon 145:100–111
14. Yan X, Hong B, Fan H, Qin F, Wang P, Zhang Z, Jiang F, Lai Y (2018) Insights into cyclable lithium loss as a key factor in accelerated capacity fade of lithiated silicon–sulfur full cells. ACS Appl Mater Interfaces 10(22):18709–18716
15. Shen T, Xia XH, Xie D, Yao ZJ, Zhong Y, Zhan JY, Wang DH, Wu JB, Wang XL, Tu JP (2017) Encapsulating silicon nanoparticles into mesoporous carbon forming pomegranate-structured microspheres as a high-performance anode for lithium- ion batteries. J Mater Chem A 5(22):11197–11203
16. Wang H, Nie G, Wang Z, Cui S, Li H, Dang L, Pu Z, Liu X, Fu A, Guo YG, Li H (2023) Carbon nanofibers with uniformly embedded silicon nanoparticles as self-standing anode for high-performance lithium-ion battery. Colloids Surf A 671:131653
17. Li H, Wang Z, Dang L, Yu K, Yang R, Fu A, Liu X, Guo YG, Li H, Zhao XS (2024) Si nanoparticles enclosed in hierarchically structured dual-component porous carbon as superior anode for lithium-ion batteries: structure formation and properties investigation. Energy Storage Mater 70:103547
18. Xie Q, Ma Y, Wang X, Zeng D, Wang L, Mai L, Peng DL (2016) Electrostatic assembly of sandwich-like Ag-C@ ZnO-C@ Ag-C hybrid hollow microspheres with excellent high-rate lithium storage properties. ACS Nano 10(1):1283–1291
19. Zhang L, Zhang J, Liu Y, Zheng P, Yuan X, Guo S (2016) Al doped-ZnO nanoparticles implanted in reduced graphene oxide with improved electrochemical properties for lithium-ion batteries. Mater Lett 165:165–168
20. Xiao C, Zhang S, Wang S, Xing Y, Lin R, Wei X, Wang W (2016) ZnO nanoparticles encapsulated in a 3D hierarchical carbon framework as anode for lithium ion battery. Electrochim Acta 189:245–251
21. Xu J, He L, Wang Y, Zhang C, Zhang Y (2016) Preparation of bi-component $ZnO/ZnCo_2O_4$ nanocomposites with improved electrochemical performance as anode materials for lithium-ion batteries. Electrochim Acta 191:417–425
22. Zhang W, Hong D, Su Z, Yi S, Tian L, Niu B, Zhang Y, Long D (2022) Tailored ZnO-ZnS heterostructure enables a rational balancing of strong binding energy and high catalytic activity of polysulfides for Li-S batteries. Energy Storage Mater 53:404–414
23. Wang B, Ren Y, Zhu Y, Chen S, Chang S, Zhou X, Wang P, Sun H, Meng X, Tang S (2023) Construction of Co_3O_4/ZnO heterojunctions in hollow N-doped carbon nanocages as microreactors for lithium–sulfur full batteries. Adv Sci 10(19):2300860
24. Gu X, Tong CJ, Wen B, Liu LM, Lai C, Zhang S (2016) Ball-milling synthesis of ZnO@ sulphur/carbon nanotubes and $Ni(OH)_2$@ sulphur/carbon nanotubes composites for high-performance lithium-sulphur batteries. Electrochim Acta 196:369–376
25. Kong Y, Luo J, Jin C, Yuan H, Sheng O, Zhang L, Fang C, Zhang W, Huang H, Xia Y, Liang C (2018) Enhanced sulfide chemisorption by conductive Al-doped ZnO decorated carbon nanoflakes for advanced Li–S batteries. Nano Res 11:477–489
26. Zhang Y, Qiu W, Zhao Y, Wang Y, Bakenov Z, Wang X (2019) Ultra-fine zinc oxide nanocrystals decorated three-dimensional macroporous polypyrrole inverse opal as efficient sulfur hosts for lithium/sulfur batteries. Chem Eng J 375:122055
27. Kalaiselvi C, Subadevi R, Wang FM, Sivakumar M (2020) Sepiolite enfolded sulfur/ZnO binary composite cathode material for Li-S battery. Front Mater 7:109
28. Yu M, Wang A, Tian F, Song H, Wang Y, Li C, Hong JD, Shi G (2015) Dual-protection of a graphene-sulfur composite by a compact graphene skin and an atomic layer deposited oxide coating for a lithium-sulfur battery. Nanoscale 7(12):5292–5298
29 Aslfattahi N, Kiai MS, Baydogan N, Samylingam L, Kadirgama K, Kok CK (2025) Integration of carbon-doped ZnO/S cathode and silicon/graphene nanoplate anode for silicon–sulfur batteries. ACS Appl Nano Mater 8:8113
30. Basiuk VA (2025) DFT calculations on single lanthanide atoms: Is the task as simple as it seems? Comput Theor Chem 1248:115170
31. Kansara S, Kang H, Ryu S, Sun HH, Hwang JY (2023) Basic guidelines of first-principles calculations for suitable selection of electrochemical Li storage materials: a review. J Mater Chem A 11(45):24482–24518
32. Kiai MS, Mansoor M, Ponnada S, Gorle DB, Aslfattahi N, Sharma RK (2022) Integration of PDAAQ and non-stoichiometric MgO as host cathode materials for lithium-sulfur batteries with superior cycle stability: density functional theory calculations and experimental validations. Energy Fuels 36(24):15199–15209
33. Guo H, Zhao Y, Lu N, Kan E, Zeng XC, Wu X, Yang J (2012) Tunable magnetism in a nonmetal-substituted ZnO monolayer: a first-principles study. J Phys Chem C 116(20):11336–11342
34. Tu ZC, Hu X (2006) Elasticity and piezoelectricity of zinc oxide crystals single layers and possible single-walled nanotubes. Physical Rev B–Condensed Matter Mater Phys 74(3):035434
35. Tu ZC (2010) First-principles study on physical properties of a single ZnO monolayer with graphene-like structure. J Comput Theor Nanosci 7(6):1182–1186
36. Wakhare SY, Deshpande MD (2019) The electronic and optical properties of monovalent atom-doped ZnO monolayers: the density functional theory. Bull Mater Sci 42(5):206
37. Topsakal M, Cahangirov S, Bekaroglu E, Ciraci S (2009) First-principles study of zinc oxide honeycomb structures. Phys Rev B–Condensed Matter Mater Phys 80(23):235119
38. Ma L, Zhang W, Wang L, Hu Y, Zhu G, Wang Y, Chen R, Chen T, Tie Z, Liu J, Jin Z (2018) Strong capillarity, chemisorption, and electrocatalytic capability of crisscrossed nanostraws enabled flexible, high-rate, and long-cycling lithium–sulfur batteries. ACS Nano 12(5):4868–4876
39. Zhou T, Lv W, Li J, Zhou G, Zhao Y, Fan S, Liu B, Li B, Kang F, Yang QH (2017) Twinborn TiO_2–TiN heterostructures enabling smooth trapping–diffusion–conversion of polysulfides towards ultralong life lithium–sulfur batteries. Energy Environ Sci 10(7):1694–1703
40. Tan ST, Chen BJ, Sun XW, Fan WJ, Kwok HS, Zhang XH. and Chua SJ. 2005 Blueshift of optical band gap in ZnO thin films grown by metal-organic chemical-vapor deposition. J Appl Phys. 98(1)
41. Rehman J, Fan X, Butt MK, Laref A, Dinh VA, Zheng WT (2021) First principles predictions of Na and K storage in layered SnSe2. Appl Surf Sci 566:150522
42. Rehman J, Lin S, Butt MK, Fan X, Khattab T, Elsayed KA, Shibl MF (2023) An overview of 2D metal sulfides and carbides as Na host materials for Na-ion batteries. Chem Eng J 461:141924
43. Yang X, Gao X, Sun Q, Jand SP, Yu Y, Zhao Y, Li X, Adair K, Kuo LY, Rohrer J, Liang J (2019) Promoting the transformation of Li_2S_2 to Li_2S: significantly increasing utilization of active materials for high-sulfur-loading Li–S batteries. Adv Mater 31(25):1901220
44. Pope MA, Aksay IA (2015) Structural design of cathodes for Li-S batteries. Adv Energy Mater 5(16):1500124
45. Urbonaite S, Poux T, Novák P (2015) Progress towards commercially viable Li–S battery cells. Adv Energy Mater 5(16):1500118
46. Pathak AD, Cha E, Choi W (2024) Towards the commercialization of Li-S battery: from lab to industry. Energy Storage Mater 72:103711

47. Park J, Kim ET, Kim C, Pyun J, Jang HS, Shin J, Choi JW, Char K, Sung YE (2017) The importance of confined sulfur nanodomains and adjoining electron conductive pathways in subreaction regimes of Li-S batteries. Adv Energy Mater 7(19):1700074
48. Hong XJ, Song CL, Yang Y, Tan HC, Li GH, Cai YP, Wang H (2019) Cerium based metal–organic frameworks as an efficient separator coating catalyzing the conversion of polysulfides for high performance lithium–sulfur batteries. ACS Nano 13(2):1923–1931
49. Zhang J, Li G, Zhang Y, Zhang W, Wang X, Zhao Y, Li J, Chen Z (2019) Vertically rooting multifunctional tentacles on carbon scaffold as efficient polysulfide barrier toward superior lithium-sulfur batteries. Nano Energy 64:103905
50. Tu S, Chen X, Zhao X, Cheng M, Xiong P, He Y, Zhang Q, Xu Y (2018) A polysulfide-immobilizing polymer retards the shuttling of polysulfide intermediates in lithium–sulfur batteries. Adv Mater 30(45):1804581
51. Zhong Y, Chao D, Deng S, Zhan J, Fang R, Xia Y, Wang Y, Wang X, Xia X, Tu J (2018) Confining sulfur in integrated composite scaffold with highly porous carbon fibers/vanadium nitride arrays for high-performance lithium–sulfur batteries. Adv Func Mater 28(38):1706391
52. Ma L, Zhu G, Zhang W, Zhao P, Hu Y, Wang Y, Wang L, Chen R, Chen T, Tie Z, Liu J (2018) Three-dimensional spongy framework as superlyophilic, strongly absorbing, and electrocatalytic polysulfide reservoir layer for high-rate and long-cycling lithium-sulfur batteries. Nano Res 11:6436–6446